Journal of Applied Fluid Mechanics, Vol. 4, Special Issue, pp. 9-20, 2011.
Available online at www.jafmonline.net, ISSN 1735-3572, EISSN 1735-3645.
DOI: 10.36884/jafm.4.03.11929

A Novel Approach to Study the Performance of Finned-Tube Heat Exchangers under Frosting Conditions

A.L. Bendaoud[1†], M. Ouzzane[2], Z. Aidoun[2] and N. Galanis[1]

[1]*Faculté de Génie, Département de Génie Mécanique, Université de Sherbrooke, 2500, boul. De l'Université, Sherbrooke, J1K 2R1, Québec, Canada.*
[2]*Ressources Naturelles Canada, 1615 Boulevard Lionel-Boulet CP 4800, Varennes, J3X 1S6, Québec, Canada.*

†*Corresponding Author Email: adlane.bendaoud@usherbrooke.ca*

(Received April 25, 2010; accepted March 13, 2011)

ABSTRACT

Frost accumulation due to moist air flowing on a refrigeration coil cold surface impacts negatively on performance. The frost layer growth has an insulating effect in terms of heat transfer and causes the increase of the air pressure drop by blocking the free flow area across the coil. In this paper a new modeling approach, accounting for heat and mass transfer as well as the hydrodynamics of the problem, is proposed. A related FORTRAN program was developed, allowing the study of a large range of complex refrigerant circuit configurations. This model predicts the dynamic behavior of a refrigeration coil under dry and frosting conditions. Comparisons were made based on the frost mass accumulation and pressure drop across the coil and the results were found to agree reasonably well with experimental results reported in the literature. The model was then applied to study an evaporator typically employed in supermarkets. In terms of refrigerant temperature glide, it was shown that the glide decrease with time because of the decrease of the refrigeration capacity of the coil during the frosting. Further, the air pressure drop is strongly affected by the variation of the free flow area.

Keywords: Modeling, Two-phase, Frost, Coil, Mass transfer, Heat transfer, Circuiting, CO_2.

NOMENCLATURE

A	Area	(m^2)
A_c	convective heat transfer area	(m^2)
A_{min}	minimum free flow area	(m^2)
C_r	capacity rate ratio	(-)
C_{min}	minimum thermal capacity rate	($W.K^{-1}$)
C_{max}	maximum thermal capacity rate	($W.K^{-1}$)
C_p	specific heat under constant pressure	($J.kg^{-1}.K^{-1}$)
D	diameter	(m)
D_c	fin collar outside diameter, $D_{ou}+2\,\delta_{fin}$	(m)
D_v	diffusion coefficient	($m^2.s^{-1}$)
f	friction factor	(-)
F_s	fin spacing	(m)
g	gravity	($N.kg^{-1}$)
h	convective heat transfer coefficient	($W.m^{-2}.K^{-1}$)
H	enthalpy	($J.kg^{-1}$)
J	Colburn factor	(-)
[J]	matrix of junctions	(-)
k	thermal conductivity	($W.m^{-1}.^oC^{-1}$)
L	length	(m)
m	mass	(kg)
$\dot{m}$	mass flow rate	($kg.s^{-1}$)
NE	number of refrigerant inlets	(-)
NF	fin density	($fins.m^{-1}$)
NJ	number of junctions	(-)
Nrow	number of rows	(-)
NS	number of refrigerant exits	(-)
NT	number of tubes	(-)
NTU	number of heat transfer units	(-)
P	pressure	($N.m^{-2}$)
Pr	Prandtl number	(-)
$\dot{Q}$	heat transfer rate	(W)
Re	Reynolds number	(-)
S_l	longitudinal tube pitch	(m)
S_t	transversal tube pitch	(m)
t	time	(s)
$T, \overline{T}$	temperature, mean temperature	(^oC)
U	overall heat transfer coefficient	($W.m^{-2}.^oC^{-1}$)
x	quality	(-)
X_{tt}	Martinelli parameter	(-)
Y_f	frost layer thickness	(m)

Greek letters

α_f	absorption coefficient	(s^{-1})
ρ	density	($kg.m^{-3}$)
Δ	variation	(-)
ω	absolute humidity	(-)

δ	thickness	(m)
θ	corrugation angle	(^{o})
ε	effectiveness	(-)
μ	dynamic viscosity of fluid	(N.s.m^{-2})
σ	surface tension	(N.m^{-1})
ν	specific volume	(m^3.kg^{-1})

Subscripts

a	air
b	bend
bc	convective boiling
d	dry
da	dry air
ev	evaporation
f	frost, frost layer
fin	fin
g	gas
in	in, inlet, inner
l	liquid, linear
lv	liquid-vapour phase change property
nb	nucleate boiling
ou	out, outlet, outer
r	refrigerant
s	surface
sat	saturation
t	total, tube
tp	two-phase
v	vapour
w	wall, water vapor

1. INTRODUCTION

Frost formation on heat exchanger surfaces is a common problem in low-temperature applications. When moist air comes into contact with cold heat exchanger surfaces whose temperature is below the freezing point, frosting occurs. The frost layer increases the overall thermal resistance, because it is a porous medium composed by air and ice; when the first layer of frost appears on the heat exchanger surface, it grows continuously, leading to the degradation of heat exchanger performance in terms of lower heat transfer and higher pressure drop. To better understand the thermal and hydrodynamic behaviour of heat exchangers operating under frosting conditions, numerical modeling represents a very cost effective approach to achieve this objective. Several research and development works on heat exchanger coils are available in the literature. Corberan *et al.* (1998) and Liang *et al.* (2001) both proposed approaches for thermal analyses of heat exchangers but little detail was given on the problem hydrodynamics and circuiting was limited to simple arrangements. Jiang *et al.* (2006) proposed CoilDesigner, a design tool in the form of easy to use software, providing a pass by pass analysis of the heat exchanger and calculating mean values of heat transfer coefficients on both air and refrigerant sides. This approximation generally leads to important differences between numerical and experimental results. CoilDesigner does not provide air-side pressure losses which may be important in large refrigeration installations. Ouzzane *et al.* (2008) and Aidoun *et al.* (2009) modeled wavy fin refrigeration coils heat using CO_2 under dry conditions. The authors used a forward marching technique to solve their conservation equations, based on the discretisation of the quality of the refrigerant. This method is not well adapted to handle complex circuiting situations. Kondepudi *et al.* (1993a, 1993b) developed an analytical model to predict the performance of finned-tube heat exchangers under frosting conditions. They considered a uniform distribution of frost on the entire heat exchanger external surface and used the ideal gas theory to calculate the mass of water diffused in the frost layer. This model used 50% ethylene-glycole/water mixture, rather than an evaporating refrigerant, in a single circuit. Seker *et al.* (2004a, 2004b) performed numerical and experimental investigations of frost formation. The authors used a custom-made heat exchanger and little information on their coil geometry is available. The experiments were performed with a large temperature difference (17 ^{o}C) between air and refrigerant. The authors used a correlation for airside heat transfer, based on their own heat exchanger data which cannot be extrapolated to other coil conditions. In this paper, a new, more general coil modeling approach accounting for complex circuiting and frost deposition is proposed. CO_2 is the refrigerant flowing through the circuits. The resulting model is built in three parts: the first part handles refrigerant flow in heat exchanger circuits and determines corresponding mass flow by solving the momentum and mass conservation equations. The second part accounts for air-refrigerant heat transfer and pressure drop, based on the e-NTU approach and appropriate correlations. The last part takes care of condensation and frost formation by computing the amount of vapour diffused in the frost layer and the mass directly contributing to increase the frost thickness. Model validation has been performed under dry and frosting conditions. In dry conditions, data obtained from an experimental CO_2 secondary refrigeration loop located in CANMETEnergy Laboratories were used (Aidoun *et* Ouzzane, 2009, and Ouzzane *et* Aidoun, 2008). In frosting conditions, the data used for validation was gathered from the open literature (Kondepudi *et* O'Neal, 1993). The model was then applied to study the performance and the operation of an evaporator typically employed in two-door refrigerated supermarket cabinets.

2. MODELING

Modeling and simulation are particularly needed for prediction and analysis purposes especially for complex systems such as circuitry in evaporator coils.

The mathematical model described in this paper is restricted to the study of the staggered and finned tube evaporator coils. Subcooled liquid, superheated vapour and two phase flow regimes may occur in these equipments and are therefore incorporated in the model. Two phase flow treatment is based on the homogeneous flow model.

CO_2 refrigerant goes through subcooled, evaporation and superheated phases from coil inlet to outlet. The mathematical model developed is based on the following main assumptions:

- System in quasi steady state conditions.
- 1-D flow of refrigerant inside the tube coil.
- Gravity forces for both air and refrigerant are neglected.
- Negligible heat losses to the surroundings.
- Uniform air velocity across each tube row.

2.1. Conservation Equations

Conservation equations of mass, momentum and energy are successively applied to a control volume element (Fig. 1). The resulting relations are summarized as:

2.1.a. Conservation Equation of Mass

$$\left(\sum \dot{m}_r\right)_{ou} = \left(\sum \dot{m}_r\right)_{in} \text{ and } \left(\dot{m}_a\right)_{ou} = \left(\dot{m}_a\right)_{in} \tag{1}$$

Pressure losses are calculated in tubes and return bends as follows:

- For tubes :

$$\left(P_r\right)_{ou} = \left(P_r\right)_{in} - \left(\Delta P_r\right)_l \tag{2a}$$

- For return bends :

$$\left(P_r\right)_{ou} = \left(P_r\right)_{in} - \left(\Delta P_r\right)_b \tag{2b}$$

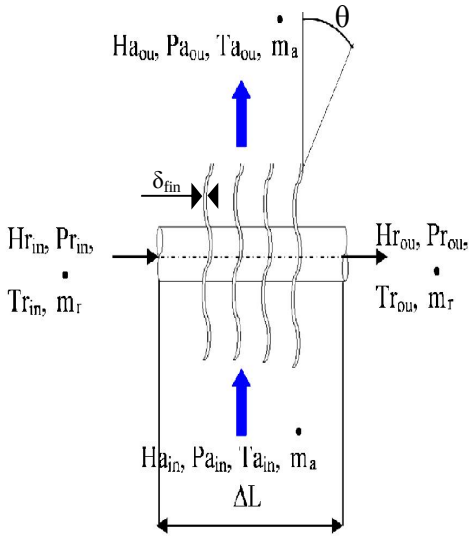

Fig. 1. Control volume element.

For single phase, subcooled liquid and superheated vapour, the Darcy-Weisbach equation is used to calculate the linear pressure drop as:

$$\left(\Delta P_r\right)_l = f.\Delta L.\frac{8.(\dot{m}_r)^2}{\rho_r.\pi^2.D_{in}^5} \tag{3}$$

The friction factor f is calculated by using the correlation given by Drew *et al.* (1932).

Pressure losses in bends are calculated by:

$$\left(\Delta P_r\right)_b = f_b.\frac{8.(\dot{m}_r)^2}{\rho_r.\pi^2.D_{in}^4} \tag{4}$$

Where the friction coefficient f_b is given by Kays *et* London (1984).

For two phase flow the linear pressure drop is calculated by the equation:

$$\left(\Delta P_r\right)_l = \left[\frac{f}{2.D_{in}}\Delta L.\nu_{tp(ou)} + (\nu_{tp(ou)} - \nu_{tp(in)})\right]G^2 \tag{5}$$

With G being the mass flow rate per unit area, and f being the friction factor coefficient determined on the basis of the homogeneous model approach reported by Rohsenow *et al.* (1998).

Pressure drop calculation in bends for two-phase flow is based on the correlations due to Geary (1975):

$$\left(\Delta P_r\right)_b = \left(f_b\right)_{tp}.\frac{L_b.x^2.G^2}{2.(\rho_r)_g.D_{in}} \tag{6}$$

L_b is the length of the bend, and $(f_b)_{tp}$ is the friction factor for a return bend calculated by:

$$\left(f_b\right)_{tp} = \frac{80352.10^{-8}.\mathrm{Re}_g^{0.5}}{\exp(0.215.C_d / D_{in}).x^{1.25}} \tag{7}$$

Where C_d is the center to center distance of bend, and Re_g is the Reynolds number based on the gas phase.

2.1.c. Conservation of Energy

The equations resulting from the energy balance are summarized as:

$$\dot{Q} = \dot{m}_r.\left[\left(H_r\right)_{ou} - \left(H_r\right)_{in}\right] \tag{8a}$$

$$\dot{Q} = \dot{m}_a.\left[\left(H_a\right)_{in} - \left(H_a\right)_{ou}\right] \tag{8b}$$

and

$$\dot{Q} = h_r.A_{in}(\overline{T_w} - \overline{T_r}) \tag{9a}$$

$$\dot{Q} = h_a.A_{ou}\left(\overline{T_a} - \overline{T_w}\right) \tag{9b}$$

Where:

$\dot{Q}$ is the heat transfer rate, h_r and h_a the heat transfer coefficients for the refrigerant and air, respectively.

2.2 CO_2 Side Heat Transfer Coefficient

For single phase, the heat transfer coefficient h_r is calculated using the correlation proposed by Petukhov and Kirillov reported by Kakaç *et al.* (1998). For two phase flow, the correlations developed by Bennet-Chen and modified by Hwang *et al.* (1997) have been used to

calculate h_r. This is based on the superposition principle, which consists of assuming that h_r is the sum of nucleate boiling coefficient h_{nb} and convection heat transfer coefficient h_{bc} as:

$$h_r = h_{nb} + h_{bc} \tag{10}$$

Where h_{nb} is given by:

$$h_{nb} = \Omega.\left(T_w - T_{sat}\left(P_l\right)\right)^{0.4}.\left(P_{sat}\left(T_w\right) - P_l\right)^{0.75}.S \tag{11}$$

And h_{bc} equation is:

$$h_{bc} = h_l.\mathrm{Pr}^{0.6}.F.(1-x)^{0.8} \tag{12}$$

h_l is the convective heat transfer coefficient for the liquid phase, calculated by Dittus-Boelter correlation (Incropera *et al.* 2002). The expressions of Ω, S and F parameters in equations (11) and (12) are given in the appendix A of the present paper.

2.3 Air Side Heat Transfer Coefficient

For air flowing over wavy plate-finned tubes, the Wang *et al.* (2002) correlations for heat transfer and pressure drop are used. Heat transfer is expressed by the Colburn coefficient as:

$$J = 0.0646.\mathrm{Re}_{Dc}^{J_1}.\left(\frac{D_c}{D_h}\right)^{J_2}.\left(\frac{F_s}{S_t}\right)^{-1.03}\left(\frac{S_1}{D_c}\right)^{0.432}.J_3 \tag{13a}$$

and

$$J = \frac{h_a.D_c}{k_a.\mathrm{Re}_{Dc}.\mathrm{Pr}_a^{1/3}} \tag{13b}$$

D_c and D_h are the fin collar outside and the hydraulic diameters respectively.

The pressure drop across the coil can be computed by the expression proposed by Kays *et* London(1984)

$$\Delta P_a = \frac{G_{\max}^2}{2\rho_{a,in}}\left[f_a\left(\frac{A_c}{A_{\min}}.\frac{\rho_{a,in}}{\rho_m}\right) + \left(\left(1+\beta^2\right)\left(\frac{\rho_{a,in}}{\rho_{a,ou}} - 1\right)\right)\right] \tag{14}$$

ρ_m calculated at average temperature of air inlet and outlet.

A_c : heat transfer area is the total air side area which contribute in the air-refrigerant heat exchange.

A_{min}: minimum free flow area is the area which one the air pass throughout the coil.

β: ratio of free-flow to frontal area (Kays *et* London, 1984).

The air friction factor f_a is calculated by the correlation proposed by Wang *et* Chi (2000)

$$f_a = 0.228\,\mathrm{Re}_{Dc}^{fl}.\left(\tan\theta\right)^{f2}\left(\frac{F_s}{S_1}\right)^{f3}\left(\frac{S_1}{D_c}\right)^{f4}.f_5 \tag{14a}$$

Air properties are calculated using the standard psychometric relations (ASHRAE, 1993).

The expressions of J_1, J_2, f_1, f_2, f_3 , f_4 and f_5 are given in the appendix B and C of the present paper.

The effectiveness-NTU method is selected for heat exchanger thermal calculations using the following additional equations:

$$\dot{Q} = \dot{Q}_{\max}.\varepsilon \tag{15}$$

$$\dot{Q}_{\max} = C_{\min}.\left(\overline{T}_a - \overline{T}_r\right)_{in} \tag{16}$$

The effectiveness ε expressions related to one phase and two phases flow are respectively:

For single phase:

$$\varepsilon = \frac{1-\exp\left\{-\left(1-C_r\right)NTU\right\}}{1-C_r.\exp\left\{-\left(1-C_r\right)NTU\right\}} \tag{17}$$

For two phase:

$$\varepsilon = 1-\exp\left(-NTU\right) \tag{18}$$

The rate of frost deposition is expressed as a loss of humidity as water vapour condenses on the cold coil surface.

$$m_f = m_{da}.\left(\omega_{in} - \omega_{ou}\right).\Delta t \tag{19}$$

The mass of the dry air is expressed as:

$$m_{da} = \frac{\dot{m}_t.\Delta t}{1+\omega_{in}} \tag{20}$$

2.4 Frost Properties

The frost distribution on the entire control volume is assumed to be uniform, and the frost layer is characterised by average properties.

When the saturated air passes throughout the coil whose surface temperature is below the dew point, the first frost layer appears. The initial conditions for frost height and density on cold surface are important as results are sensitive to their selection (Shokouhmand *et al.*, 2009). Jones and Parker (1975) tested the initial conditions by changing the values of the initial frost thickness and density, they found that the prediction results of the frost growth rate would not be affected significantly if the initial frost thickness value approaches a low value (~ 2 x 10^{-2} mm). They also found that as long as the initial value of the frost density is significantly smaller than the frost density during growth, it will not affect the solution for the frost growth rate of densification, the recommended value being (~ 30 kg.m^{-3}). Hence, in this work, the initial conditions for the frost temperature, thickness and density are fixed as:

$$\begin{aligned} T_f^0 &= T_w \\ \delta_f^0 &= 2.10^{-5}\,m \\ \rho_f^0 &= 30\,kg/m^3 \end{aligned} \tag{21}$$

The water vapour transferred, from moist air to the frost surface, increases both the frost density and thickness. This phenomenon can be expressed as:

$$m_f = m_\delta + m_\rho \tag{22}$$

The mass flux from the frost density absorbed into frost layer is given by Lee *et al.* (1997):

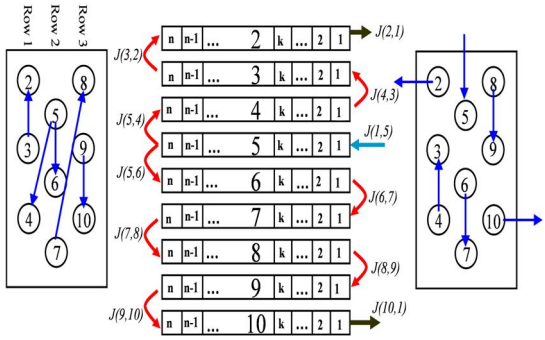

Fig. 2. An example of circuiting configuration and conventions.

$$m_\rho = \int_{\delta_f=0}^{\delta_f=Y_f} \alpha_f \rho_w .\Delta t.d\delta_f \tag{23}$$

Were α_f represents an absorption coefficient calculated by:

$$\alpha_f = D_v.\left[\frac{\cosh^{-1}}{\delta_f}\left\{\frac{\rho_{w,sat}(T_{f,s})}{\rho_{w,sat}(T_w)}\right\}\right]^2 \tag{24}$$

The thermal conductivity, valid for $30 \le \rho_f \le 400 \quad kg.m^{-3}$, is given by:

$$k_f = 0.132 + 3.13.10^{-4}.\rho_f + 1.6.10^{-7}.\rho_f^2 \tag{25}$$

The diffusion coefficient D_v, valid for $-50 \le \overline{T}_a \le +20\ ^\circ C$, is given by:

$$D_v = \left(a + b\overline{T}_a + c\overline{T}_a^2 + d\overline{T}_a^3\right).10^{-5} \tag{26}$$

With

$a = 2.219928$ $\qquad$ $c = -0.0000065$

$b = 0.0137779$ $\qquad$ $d = -5.32937434.10^{-7}$

The frost density and thickness for each time interval are calculated as follow, Kondepudi *et al.* (1993a):

$$\Delta\rho_f = \frac{\dot{m}_\rho \Delta t}{A_{c,d}\delta_f} \tag{27}$$

And

$$\Delta\delta_f = \frac{\dot{m}_\delta \Delta t}{A_{c,d}\rho_f} \tag{28}$$

$A_{c,d}$: convective heat transfer area at dry condition.

3. RESOLUTION PROCEDURE

This simulation model is intended to cover a large range of operating conditions and handle complex circuiting configurations. In order to achieve this objective, the solution procedure is based on the adoption of an original strategy for the convention of numbering and localizing the tubes, identifying refrigerant entries, exits, tube connections, as well as control volume variables. Rows are counted according to the air flow direction.

J(I,K) is a matrix indicating the presence or absence of a junction between two tubes; the coordinates I and K indicate the direction of flow: incoming and destination, respectively. The values of J(I,K) are:

$$J(I,K) = \begin{cases} 0 & no\ \ connection\ between\ I\ and\ K\ tubes \\ 1 & connection\ between\ I\ and\ K\ tubes \end{cases}$$

Figure 2 shows an example of a heat exchanger with 9 tubes arranged in three rows and three lines with one entrance in tube 5 and two exits in tubes 2 and 10. J(1,5) means that the refrigerant enters in tube 5 and exits from tubes 2 and 10 J(2,1) and J(10,1)). J(4,3) is the junction between tubes 4 and 3 and the flow comes from tube 4 and goes through tube 3.

Tubes are numbered starting from 2 at the top and the number one is reserved to external entrance or exit.

For mass flow rate, pressure and temperature variables, the following conventions have been used:

m(I,K) is the mass flow rate in the junction J(I,K). When K=I, m(I,I) is the mass flow rate in tube I.

P(I,k) is the pressure in the volume control element k in the tube I.

T(I,k) is the temperature in the volume control element k in the tube I.

Each tube I is divided into n volume control elements, starting either from the left or from the right, according to the refrigerant flow direction entrance

For this purpose, a parameter DIR(I) having a value of 1 or -1 is allocated to each tube. In Fig. 2, the direction of the upper entrance tube is chosen as a positive reference (DIR(I)=1), and
DIR(5)=DIR(3)=DIR(7)=DIR(9)= +1
DIR(2)=DIR(4)=DIR(6)=DIR(8)=DIR(10)= -1

The calculation procedure is based on an iterative method consisting for the first step in calculating the hydrodynamic field (mass flow rate and pressure). Then, the conservation equations of mass and momentum are applied to each tube and connection which leads to a total of **3*NT+NJ** equations. **NT** and **NJ** are the total numbers available of tubes and junctions respectively. In the example shown by Fig. 2: **NT=9** and **NJ=8**. This leads to a total number of **3*9+8=35** equations**.**

In general, the total number of the unknown variables is for:

- Mass flow rate **NT+ NJ** which is **9+8=17** for the example shown in Fig. 2.

- Pressure **2*NT** which is **2*9=18** for the example shown in Fig. 2, with the assumption that outlet pressures are equal.

Equations for mass flow rate and pressure are grouped together; the matrix formula is then written as:

$$\begin{bmatrix} [A_m] & [0] \\ [0] & [A_p] \end{bmatrix} \begin{bmatrix} (\dot{M}) \\ (P) \end{bmatrix} = \begin{bmatrix} (B_m) \\ (B_p(\dot{m})) \end{bmatrix} \tag{29}$$

$[A_m]$ and $[A_p]$ are the matrix coefficients for mass flow rate and pressure.

$(\dot{M})$ and (P) are the mass flow rate and the pressure vectors.

(B_m) and $B_p(\dot{m})$ are the second vectors for mass flow rate and pressure, the latter depending on the former. Equation (29) can be written as:

$$[A].(X) = (B(X)) \tag{30}$$

where (X) is the vector of variables, including pressure and mass flow rate.

The system obtained through the above equation is nonlinear and the Newton-Raphson iterative method based on the calculation of the Jacobian matrix and its inverse is used (Kiusalaas, 2005).

The main steps of the solution procedure are presented by the flow chart represented in Fig. 3.

Once geometric, temporal parameters and inlet thermodynamic data, as well as circuitry configuration parameters are read, the program calculates flow direction and priority vectors DIR(I) and PRIO(I) needed for the organisation of the elements matrix in equation 30, according to the priority of calculation. Using this equation, a preliminary hydrodynamic calculation is performed by the subroutine HYDRO which sets refrigerant mass flow rate and pressure vector (X). The procedure continues by defining the thermodynamic state of refrigerant using subroutine REFPROP, and then the thermal calculation is performed according to the three possible cases:

- Two-phase: calculations are made according to the steps on the right branch of the flowchart.

- Subcooling: is treated according to the steps on the left branch.

- Superheat: no calculations are performed since there is no evaporation.

The elements of the new vectors ($\dot{m}$) and (P_{new}) are calculated using the subroutine HYDRO and the calculation process is repeated until convergence of the refrigerant mass flow rate is reached.

When both hydrodynamic and thermal convergence is obtained, the subroutine HUMI is called to compute the relative humidity in the air inlet and outlet of each volume element. These relative humidities are stored in the matrices [Φ_{in}] and [Φ_{ou}] respectively. The program then checks, for each volume element if the conditions of frost formation are verified, i.e. saturated air and T_s below the freezing point. For the elements under the dew point temperature, the subroutine computes the mass of the frost formed and both diffused (m_ρ) and solidified (m_δ) mass parts are calculated. Afterwards, the program calls the subroutine UPCOILGEO to update the geometry configuration of the heat exchanger (tube outer diameter, fin thickness, convective heat transfer area and free flow area) and stores the information in respective matrices. Then, by considering the new geometry of the heat exchanger,

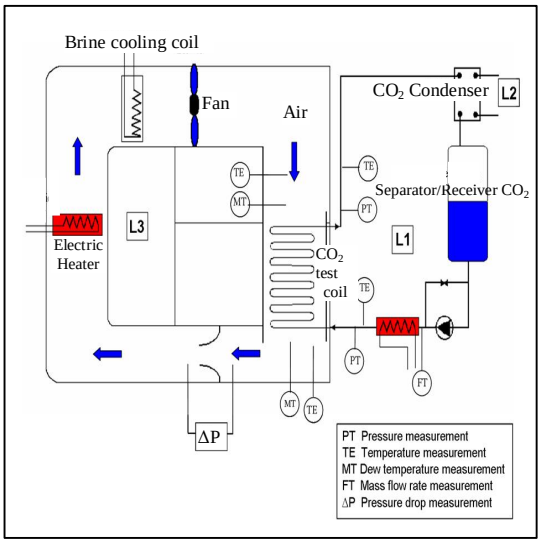

Fig. 4. Schematic diagram of test set-up.

resulting from frost deposition over a time step, the hydrodynamic, thermal and prychrometric calculations process are reapeted for each time step Δt until the total working period of the heat exchanger is covered.

4. RESULTS AND COMPARISON WITH REPORTED EXPERIMENTAL DATA

In order to validate the present model, the results have first been compared with the available information for dry conditions. Preliminary comparisons were performed with numerical results from a previous model developed by Ouzzane *et* Aidoun (2008) and further validation was achieved by using experimental results from the CanmetENERGY test bench. This experimental set-up shown in Fig. 4, complies with ASHRAE standards (2000a, 2000b) for forced air cooling and

heating coils. Evaporating carbon dioxide is the working fluid in the secondary loop (L1), which includes a CO_2 pump, a mass flow meter, a CO_2-air coil with aluminum wavy fins and copper tubes, a brazed plate condenser and a reservoir for CO_2 condensate. The loop is well instrumented for the purpose of heat and mass transfer balances and fluid flow. For a flexible control of temperature and capacity, a brine loop (L2) was used to cool down the CO_2 condenser. The temperature control of this loop is achieved by a mechanical refrigeration system (L3). Loop (L1) is located in a closed room with two compartments corresponding to inlet and outlet of the coil: air flows from one compartment to the other through a duct enclosing the coil. Air circulation is maintained by a blower. The compartments are well insulated in order to reduce infiltration from outside air and moisture. More details on the experimental set up may be found in Aidoun *et* Ouzzane (2009). The accuracy of the temperature was within 0.05 °C, absolute pressure was read within ± 0.3kPa, the pressure differential at the coil within ± 5 Pa, and air flow rates within 2 %. Experiments were conducted with CO_2 inlet temperatures and mass flow rates in the ranges of -35 °C to -15 °C and 0.014 kg/s to 0.044 kg/s, air temperatures and approach velocities in the ranges of -30 °C to -9 °C and 1 m/s to 3 m/s respectively.

Table1. Input conditions for validation.

	Mass flow rate (kg/s)		Inlet temperature (C)		Inlet pressure (kPa)	
	Air	CO_2	Air	CO_2	Air	CO_2
Case 1	0.5865	0.027	-15.5	-26.07	101.325	1624.7
Case 2	0.6070	0.019	-15.6	-26.93	101.325	1580.5
Case 3	0.6090	0.015	-20.3	-24.03	101.325	1732.8
Case 4	0.5997	0.044	-10.1	-23.05	101.325	1787.5
Case 5	0.6063	0.032	-21.84	-25.91	101.325	1632.0

Table 2. Comparisons of results with numerical results from previous model and with an experimental data.

		Capacity (W)		Outlet quality	ΔP (kPa)	Outlet temperature (^oC)		Outlet relative humidity (%)
		Air	CO_2	CO_2	CO_2	Air	CO_2	Air
CASE 1	**Present model**	4091.0	4112.9	52.8 %	170.2	-22.4	-29.4	-
	Previous model	4438.3	4530.6	58.0 %	195.2	-23.0	-29.9	-
	Experiments	4083.3	-	51.4 %	171.6	-22.4	-29.6	66.0
CASE 2	**Present model**	4444.6	4435.2	80.7 %	152.5	-22.9	-30.0	-
	Previous model	4811.5	4914.1	89.0 %	149.6	-23.5	-29.9	-
	Experiments	4471.0	-	75.0 %	132.2	-22.9	-29.6	65.6
CASE 3	**Present model**	1402.4	1379.1	32.5 %	29.3	-22.6	-24.5	-
	Previous model	1557.2	1550.0	36.5 %	38.6	-22.8	-24.8	-
	Experiments	1495.9	-	35.5 %	44.4	-22.7	-24.9	76.0
CASE 4	**Present model**	5588.8	5590.6	45.3%	195.0	-19.4	-26.6	-
	Previous model	5869.4	5683.8	47.5%	398.9	-19.8	-30.8	-
	Experiments	5458.0	-	43.5 %	303.4	-19.1	-28.8	54.7
CASE 5	**Present model**	1708.4	1709.9	18.4%	42.0	-24.6	-26.7	-
	Previous model	1871.1	1798.4	20.0 %	107.7	-24.9	-28.0	-
	Experiments	1640.0	-	18.3 %	97.0	-24.5	-27.8	81.5

Table 3. Coil specification and operating condition (Kondepudi *et* O'Neal, 1993a, 1993b)

Description	**Value**
Weidth (m)	0.4572
Height (m)	0.4572
Depth (m)	0.022
Fin density (fins/meter)	710
Fin thickness (mm)	0.12
Fin type	Flat, aluminium
Inner diameter (mm)	9.195, copper
Outer diameter (mm)	9.525
Number of rows	1
Number of tubes par row	18
$(T_{air})_{in}$ (°C)	0.0
Φ_{in} (%)	80.0
Face velocity (m/s)	0.762
$\dot{m}_r$ (l/min)	24.61
Refrigerant type	50% ethylene glycol /water
$(T_r)_{in}$ (°C)	-15.0

For comparison purposes, five different experimental cases were selected, with their operating conditions sumarized in Table 1.

For all the five cases, presented in this table, the refrigerant is entering the coil in a saturated state with an assumed quality of 0 %. The results in Table 2, show that the coil capacity predicted by the present model is in good agreement with the experimental data, the maximum discrepancy being less than 6.5 %. Comparison with the previous model, due to Ouzzane *et* Aidoun (2008) shows differences of up to 14 %. The results show also that the refrigerant pressure drop predicted by the present model is in good agreement with the experimental data except for the fifth case where the discrepancy between predictions and experiments is equal to 57 %. Among possible reasons are the cumulative errors resulting from the iterative process applied with correlations for pressure drop whose overall uncertainty is in the range ± 67 % (Rin *et al.*, 2006) while for heat transfer coefficient this

uncertainty on the predictions is within ± 40 % range (Hwang *et al.*, 1997). In the analysis performed by Ouzzane *et* Aidoun (2008), the pressure drop for saturated refrigerant flow is strongly affected by the quality of the refrigerant. Since the iterative process in the present approach is based on tube length increments, and because quality is a computation result, it is possible that sudden jumps in quality occur towards the end of the evaporation process and result in correspondingly high departures of the pressure drop

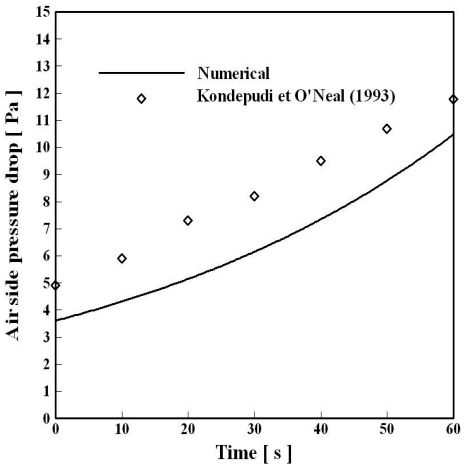

Fig.5. Variation of air side pressure drop across the coil

outside the range covered by the correlations used.

For the frosting case, simulations are conducted according to the test conditions of Kondepudi *et* O'Neal (1993b). The geometric specifications of the heat exchanger and the operational conditions are summarised in Table 3. In the experimental results shown in Fig. 5, the air side pressure drop increases with time. The increasing trend is due to the frost height continuing to grow, thus reducing

the flow passage cross-sectional area which decreases by nearly 65%, inducing an increase of both the air Reynolds number and the friction factor. Experimental values for pressure drop increase from 4.9 Pa to 10.77 Pa at the end of the experiment. The present model predicts the experimental results fairly well.

In the results shown in Fig. 6, the total mass of frost formed in the heat exchanger increases with time. The numerical results show that the part of the condensed water diffused in the frost layer increases the frost density, reaching a value of 496 $kg.m^{-3}$. This density corresponds to 0.326 $W.K^{-1}.m^{-1}$ for the thermal conductivity of the frost.

5. TYPICAL REFRIGERATION APPLICATION

An example of simulation at low temperature was performed on a wavy fin-and-tube heat exchanger typically used in supermarket applications Fig.7. The rows of the coil are disposed in staggred configuration and the air and refrigerant are flowing in counter-flow.

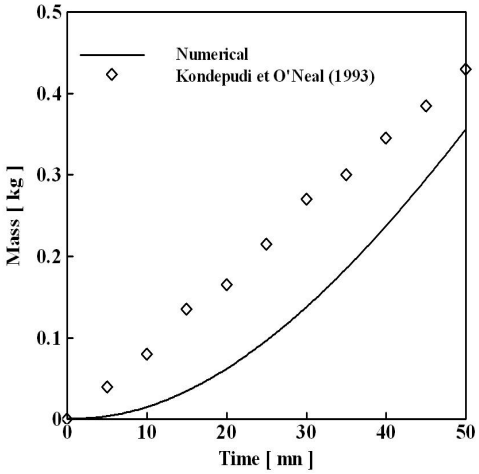

Fig.6. Frost mass accumulation comparison.

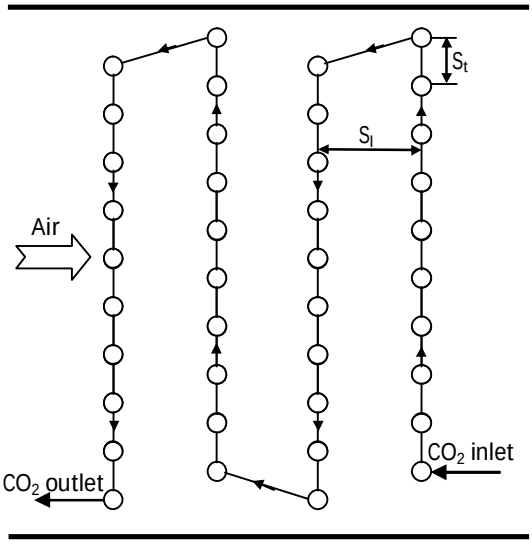

Fig. 7. CO_2 circuit of the heat exchanger.

Table 4. Geometrical data and operational conditions.

Description	**Value**
Configuration	Staggred
Refrigerant type	CO_2
Number of tubes per row	10
Numer of tubes row	4
S_t (mm)	31.8
S_l (mm)	27.8
Fin thickness (mm)	0.19, aluminium
Tube length (m)	0.61, copper
Tube inner diameter (mm)	9.525
Tube outer diameter (mm)	12.7
Fin density (fins/meter)	70
Inlet relative humidity (%)	90
$(T_{air})_{in}$ (°C)	-15
Air flow rate ($kg.s^{-1}$)	0.6
$(T_r)_{in}$ (°C)	-25
CO_2 flow rate ($kg.s^{-1}$)	0.03
Fin type	Wavy
Corrugation angle (°)	8

The geometry, core dimensions and relevant operating conditions are summarized in Table 4, were realistic values taken from a manufacturer's specifications manual. Profiles of refrigeration capacity, frost growth, convective heat transfer area, free flow area, air pressure drop and CO_2 temperature distribution are presented in Figs. 8, 9, 10, 11, 12 and 13 respectively.

Figure 8 is the variation of the refrigeration capacity delivered by the coil, showing that the capacity decreases, due to frost accumulation on the coil. This is explained by the fact that a thicker frost layer on heat exchanger surface leads to a greatly reduced heat transfer area and increased resistance to heat transfer. This results in a greater reduction of the heat transfer coefficient and of total heat transfer.

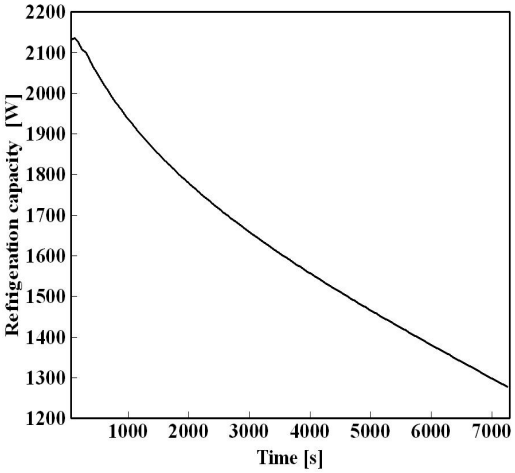

Fig.8. Variation of the refrigeration capacity.

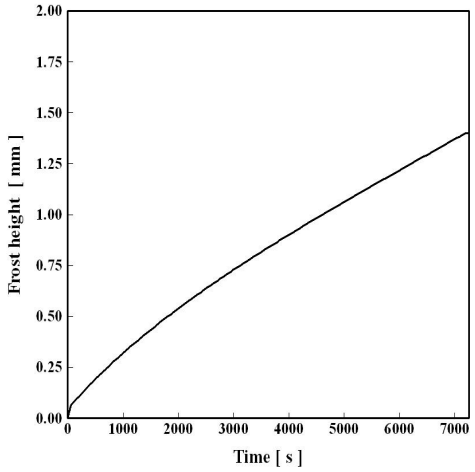

Fig.9. Frost accumulation

Figure 9 shows the variation of the mean frost height formed over the coil. The mean frost height is calculated from the frost deposited on the entire tube rows of the heat exchanger. At t = 2400 s (40 mn), the mean frost height reached 50 % (0.6179 mm) of its final value attained at t = 120 mn (end of the process). This phenomenon is explained by the fact that at the start of the process (dry case) the heat exchanger delivers a maximum refrigeration capacity thereby producing correspondingly high quantities frost.

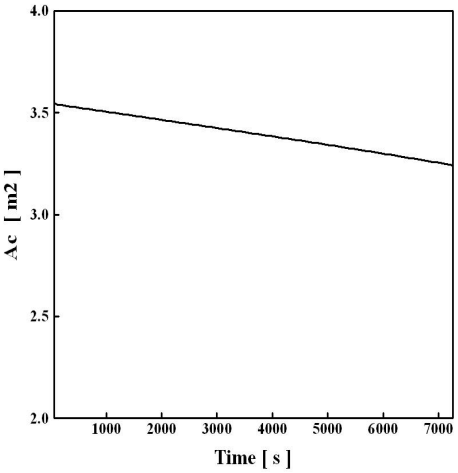

Fig.10. Variation of the total convective heat transfer area.

In proportion, as frost accumulates on the airside heat transfer surface, thermal resistance increases, reducing the refrigeration capacity delivered and slowing down frost deposition. Figure 10 shows the variation of the total convective heat transfer area (A_c). The total convective heat transfer area represents the total air side area which contributes to the air-CO_2 heat exchange. At the end of the process, the convective heat transfer area is reduced by 9 % if compared to the convective heat transfer area for the dry condition. This variation is due to the fact that frost formation on the tubes and fins increases external diameters, reducing the convective fin area and simultaneously increases fin thickness, thereby reducing the convective heat transfer area of the tubes.

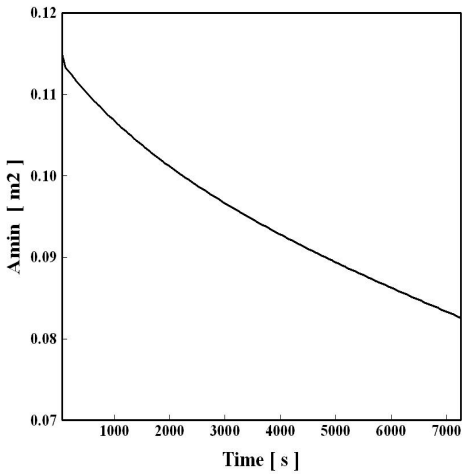

Fig.11. Variation of the mean minimum free flow area.

Figure 11 shows the variation of the mean free flow area (A_{free}) calculated from the total free flow area of the tube rows. The maximum and minimum values of the mean free flow area corresponds to the dry and frosted (at the end of the process) cases respectively. This variation is the result of the frost accumulation on

the air side area of the heat exchanger. This accumulation enhance the fin thickness and the outer tube diameter which reduce the air section flowing. In the treated example, A_{free} is reduced by 28 % at the end of the process.

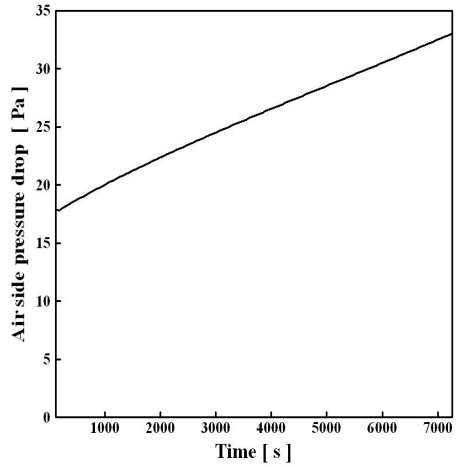

Fig.12. Variation of air pressure drop.

Figure 12 shows the variation of the air pressure drop across the coil. Pressure drop is shown to increase due to frost formation in the coil which adds a supplementary heat transfer resistance and decreases both the convective heat transfer area and the free flow area. The variations of these two areas affect strongly the air pressure drop and overall heat transfer as shown in Fig.13 and discussed in the next section. In the equation (14), used to compute ΔP_a across the coil (Kays *et* London, 1984), both the core friction and contraction effect parts are dependant to the variation of the ratio A_c to A_{free}. The variation of this ratio by the accumulation of the frost in the coil increases rapidly the air pressure drop.

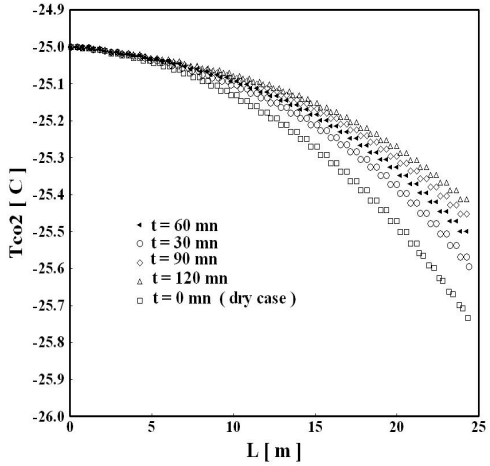

Fig.13. Variation of the CO_2 temperature at several periods.

The heat exchanger studied has one refrigerant circuit arranged in four rows and 40 tubes with a total length 'L' of 24.4 m. The refrigerant temperature at inlet is -25 ^oC, and Figure 13 shows the refrigerant temperature profile over the coil at different time steps: t = 0 mn (dry case), 30 mn, 60 mn, 90 mn and 120 mn. The CO_2 temperature difference between the inlet and the outlet of the coil represents the temperature glide corresponding to the pressure drop when phase change is taking place. The higher temperature glide corresponds to the dry case performance when the maximum refrigeration capacity is delivered and the higher refrigerant quality at the exit is obtained relate to heat exchanger area. As shown by Aidoun *et* Ouzzane (2009) the increasing quality of the refrigerant flow as it evolves through the circuit, affect strongly its pressure drop. When frost formation occurs, the coil refrigeration capacity and the exit refrigerant quality both decrease, due to less heat transfer which eventually results in reduced refrigerant pressure drop and low temperature glide.

6. CONCLUSION

A mathematical model was developed to calculate the quasi-permanent hydrodynamic and thermal characteristics of circuited, fin-and-tube refrigeration heat exchangers, working under dry (i.e. without condensation) and frosting conditions. Validation for dry conditions was performed with experimental data obtained on a refrigeration facility in Canmet Energy, Varennes, and for frosted conditions, the data used were obtained from the literature. Comparison of numerical predictions and experimental results were shown to be in very good agreement. Simulations based on this model, can therefore be performed to study heat exchanger operation and performance, with complex circuit configurations and different refrigerant flow paths. Preliminary results obtained on a typical supermarket coil show that the frost formation degrades the performance of the heat exchanger by reducing the air-refrigerant heat transfer and by increasing the airside pressure drop. It is intended in future work, to fully use the flexibility offered by this tool to generate results under different condensation and frosting conditions, with geometric configurations, circuit arrangement and refrigerant flow path selection as parameters for optimal geometry and performance selection.

REFERENCES

Aidoun Z. and Ouzzane M. (2009). *A model application to study circuiting and operation in CO_2 refrigeration coils*, Applied Thermal Engineering vol. 29, pp. 2544-2553.

ASHRAE Standard (2000a). *Standard methods for laboratory measurement*, vol.41.2-1987(RA 92).

ASHRAE (1993). *ASHRAE handbook of fundamentals, SI Edition*, ch. 6, pp.1-17, Atlanta, Georgia, U.S.A.

ASHRAE Standard (2000b). *Methods of testing forced circulation air cooling and air heating coils*, p. 33-78.

Bendaoud A.L., Ouzzane M., Aidoun Z. and Galanis N. (27, 28, 29 Mars 2009). Nouvelle approche pour l'étude des évaporateurs de type : tube à ailettes

air/co_2 à basse température, *Proceeding des 14emes Journées Internationales de Thermique (JITH)*, papier No 18, Djerba, Tunisie.

Corberan J.M. and Melon M.G. (1998). *A modeling of plate finned tube evaporators and condensers working with R134A*, Int. J. of refrigeration vol. 21, No.4 , pp. 273-283.

Drew T.B., Koo E.C. and Mc Adams W.H. (1932). *The friction factors for clean round pipes*, Trans. AIChE vol. 28-56.

Geary D.F. (1975). *Return bend pressure drop in refrigeration systems*, ASHRAE Transactions, vol. 81, No. 1, pp. 250-264.

Incropera F.P. and DeWitt D.P. (2002). *Fundamentals of heat and mass transfer*, John Wiley and Sons, 5th edition, NY.

Hwang Y., Kim B.H. and Radermacher R. (Nov. 1997). *Boiling heat transfer correlation for carbon dioxide*, IIR international conference, Heat Transfer Issues in Natural Refrigeration.

Jiang H., Aute V. and Radermacher R. (2006). *CoilDesigner: A general-purpose simulation and design tool for air-to-refrigerant heat exchangers*, Int. J. of refrigeration vol. 29, pp. 601-610.

Jones and Parker J.D. (1975). *Frost formation with varying environmental parameters*. J. Heat Transfer vol. 97, pp. 255–259.

Kakaç S., Liu H. (1998). *Heat exchangers, Selection, Rating and Thermal Design*, CRC Press LLC.

Kays, W.M. and London, A.L. (1984). *Compact heat exchangers*, 3rd ed., NewYork, McGraw-Hill.

Kiusalaas J. (2005). *Numerical methods in engineering with python*, CAMBRIDGE University Press, pp.159.

Kondepudi S.N., O'Neal D.L. (1993a). *Performance of finned-tube heat exchangers under frosting conditions: I. Simulation model*, Int.J. Refrigeration vol. 16, No. 3, pp. 175-180.

Kondepudi S.N. and O'Neal D.L. (1993b). *Performance of finned-tube heat exchanger under frosting conditions: II. Comparaison of experimental data with model*, Int.J. Refrigeration vol. 16, No. 3, pp. 181-184.

Lee K.S., Kim W.S. and Lee T.H. (1997). *A one-dimensional model for frost formation on a cold flat surface*, Int. J. Heat Mass Transf. vol. 40 No.18, pp. 4359-4365.

Liang S.Y., Wong T.N. and Nathan G.K. (2001). *Numerical and experimental studies of refrigerant circuitry of evaporators coils*, Int. J. of refrigeration vol. 24, pp. 823-833.

Ouzzane M. and Aidoun Z. (2008). *A numerical study of a wavy fin and tube CO2 evaporator coil*, Heat transfer engineering vol. 29, No. 12, pp. 1008-1017.

Rin Y., Jae H.H., Yongchan K. (2006). *Evaporative heat transfer and pressure drop of R410A in microchannels*, International Journal of Refrigeration, vol. 29, pp. 92-100.

Rohsenow, W.M., Hartnett, J.P. and Cho and Y.I. (1998). *Handbook of Heat Transfer*, Third Edition, Mc Graw Hill, New York, pp. 17.89-17.97.

Seker D., Karatas H. and Egrican N. (2004a). *Frost formation on fin-and-tube heat exchangers. Part I—Modeling of frost, formation on fin-and-tube heat exchangers*, Int.J. Refrigeration vol.27, No.4, pp.367-374.

Seker D., Karatas H. and Egrican N. (2004b). *Frost formation on fin-and-tube heat exchangers. Part II—Experimental investigation of frost formation on fin- and- tube heat exchangers*, Int.J. Refrigeration vol.27, No.4, pp. 375-377.

Shokouhmand H., Esmaili E., Veshkini A., Sarabi Y. (1st January 2009). *Modeling for predicting frost behavior of a fin-tube heat exchanger with thermal contact resistance*, ASHRAE Transactions, pp. 538-551.

Wang, C.C., Hwang, Y.M. and Lin, Y.T. (2002). *Empirical correlations for heat transfer and flow friction characteristics of herringbone wavy fin-and-tube heat exchangers*, Int. J. of refrigeration, vol. 25, pp.673- 680.

APPENDIX A

Expression to calculate the parameters Ω, S and F of equations (11) and (12)

$$\Omega = 0.00122\left(\frac{k_l^{0.79}.Cp_l^{0.5}.\rho_l^{0.49}}{\sigma^{0.6}\mu_l^{0.29}h_{lv}^{0.24}\rho_v^{0.24}}\right) \tag{A.1}$$

$$S = \frac{1-EXP\left(-F.h_l X_0/k_l\right)}{F.h_l X_0/k_l} \tag{A.2}$$

$$X_0 = 0.05\left[\frac{\sigma}{g\left(\rho_l-\rho_v\right)}\right]^{0.5} \tag{A.3}$$

$$F = \begin{cases} 1.0 & if \quad X_{tt} \geq 10 \\ 2.0\left(0.213+X_{tt}^{-1}\right)^{0.736} & if \quad X_{tt} < 10 \end{cases} \tag{A.4}$$

$$X_{tt} = \left(\frac{1-x}{x}\right)^{0.9}\left(\frac{\rho_v}{\rho_l}\right)^{0.5}\left(\frac{\mu_l}{\mu_v}\right)^{0.1} \tag{A.5}$$

APPENDIX B

Expression to calculate the parameters J_1 , J_2 and J_3 of equation (13)

$$J_1 = \xi_1 - 0.302 Nrow^{-0.24}.\xi_2 \tag{B.1}$$

$$J_2 = \xi_3.Nrow^{-0.166-1.08\tan\theta}\left(\frac{F_s}{S_t}\right)^{-0.174\ln(0.5\,Nrow)} \tag{B.2}$$

$$J_3 = \left(\tan\theta\right)^{-0.692} Nrow^{-0.737} \tag{B.3}$$

$$\xi_1 = -0.0545 - 0.0538\tan\theta \tag{B.4}$$

$$\xi_2 = \left(\frac{F_s}{S_1}\right)^{-1.3}\left(\frac{S_1}{S_t}\right)^{0.379}\left(\frac{S_1}{D_h}\right)^{-1.35}\tan\theta^{-0.256} \tag{B.5}$$

$$\xi_3 = -1.29\left(\frac{S_1}{S_t}\right)^{1.77-9.43\tan\theta}\left(\frac{D_c}{D_h}\right)^{0.229-1.43\tan\theta} \tag{B.6}$$

APPENDIX C

Expression to calculate the parameters f_1, f_2, f_3 , f_4 , f_5 and f_6 of equation (14)

$$f_1 = -0.141\left(\frac{F_s}{S_1}\right)^{0.0512}\left(\tan\theta\right)^{-0.472}.f_6 \tag{C.1}$$

$$f_2 = -0.562\left(\ln\left(\mathrm{Re}_{Dc}\right)\right)^{-0.0923} Nrow^{0.013} \tag{C.2}$$

$$f_3 = 0.302\,\mathrm{Re}_{Dc}^{0.03}.\left(\frac{S_1}{S_t}\right)^{0.026} \tag{C.3}$$

$$f_4 = -0.306 + 3.63\tan\theta \tag{C.4}$$

$$f_5 = \left(\frac{D_c}{D_h}\right)^{0.383}\left(\frac{S_1}{S_t}\right)^{-0.247} \tag{C.5}$$

$$f_6 = \left(\frac{S_l}{S_t}\right)^{0.35}\left(\frac{S_t}{D_h}\right)^{0.449\tan\theta} Nrow^{-0.049+0.237\tan\theta} \tag{C.6}$$